

Numerical Analysis of a TMCZ Silicon Growth Furnace by Using a 3D Global Model

劉, 立軍
九州大学応用力学研究所

柿本, 浩一
九州大学応用力学研究所

<https://doi.org/10.15017/3551>

出版情報 : 九州大学応用力学研究所所報. 127, pp.39-47, 2004-09. Research Institute for Applied Mechanics, Kyushu University

バージョン :

権利関係 :

Numerical Analysis of a TMCZ Silicon Growth Furnace by Using a 3D Global Model

Lijun LIU* and Koichi KAKIMOTO*

E-mail of corresponding author: lxl@riam.kyushu-u.ac.jp

(Received July 30, 2004)

Abstract

Three-dimensional (3D) global simulations were carried out for a small Czochralski (CZ) furnace for silicon crystal growth with a recently developed global model. The furnace is placed in a transverse magnetic field. The convective, conductive and radiative heat transfers in the entire furnace were solved in a three-dimensionally conjugated way. Three-dimensional features of the melt flow and thermal field in the furnace due to the influence of a transverse magnetic field were reasonably reproduced in the modeling for cases in which the crystal and crucible are rotating or are not rotating. The effects of crystal and crucible rotations on the melt-crystal interface shape and the 3D thermal field within the furnace were analyzed. The model was proved to be an effective and powerful tool for analyzing a silicon CZ furnace characterized with three-dimensionality.

Key words : *Computer simulation, Global modeling, Czochralski method, Transverse Magnetic field, Semiconducting silicon*

1. Introduction

Application of magnetic fields in silicon CZ growth processes is an effective method for controlling the melt-crystal interface shape and the melt convection in a crucible, and therefore for improving crystal quality. Active control by applying a transverse magnetic field to silicon CZ growth processes (TMCZ) is obtaining growing attention in academia and industry. The melt flow in a crucible and, hence, the global thermal field within the furnace are principally three-dimensional under the influence of a transverse magnetic field. On the other hand, since the shape of the melt-crystal interface is of great interest for practical growth and the growth furnace is a highly nonlinear system, three-dimensional global modeling is obviously necessary. However, although there are many excellent published works on numerical modeling of a

TMCZ silicon growth¹⁻⁶⁾, most of them are limited to the three-dimensional melt flow by the imposition of a flat melt-crystal interface and thermal boundary conditions in their respective models. This is because of the very high requirement of computing resources for a fully 3D global modeling.

Most recently, Liu and Kakimoto⁷⁾ developed a novel 3D global model that makes 3D global modeling be feasible with moderate requirements of computer resources and computation time. By using this model, the convective, conductive and radiative heat transfers in the entire furnace were solved in a three-dimensionally conjugated way. The entire thermal field within a furnace, as well as the 3D melt-crystal interface shape, can be simulated, and the heater input power can be predicted, only if a set of basic input parameters is provided in the modeling. For the purpose of a better understanding of the realistic phenomena and the physics of a TMCZ silicon growth process, the model was applied in analyzing a small

* Research Institute for Applied Mechanics, Kyushu University

TMCZ furnace in this paper.

2. Theory of 3D global modeling

2.1 The discrete system of 3D global modeling

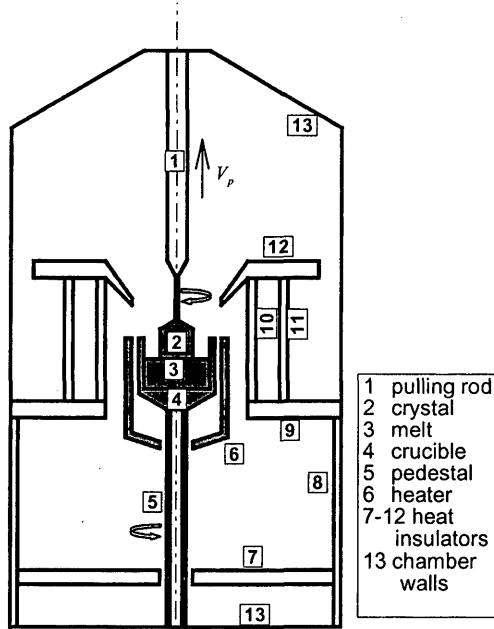


Fig. 1 Configuration and domain partition of a CZ furnace

The configuration of a small CZ furnace that was investigated in this study is illustrated in Fig. 1. The geometry of the furnace is axisymmetric. All of the constituents of the furnace are subdivided into a set of block regions as shown in Fig. 1, in which subdivision resulted in a total of thirteen block regions. Each of these block regions is covered by a structured grid.

In order to perform 3D global modeling with moderate requirements of computer memory and computation time, a mixed 2D/3D space discretization scheme was developed⁷⁾. Following this scheme, the components in the core region of the furnace, namely, the 3D domain, are discretized in a three-dimensional way, while the domains away from the core region, namely, the 2D domain, are discretized in a two-dimensional way. This is based on (1) the fact that the three-dimensionality of the system is induced originally in the melt flow and (2) the observation that it rapidly becomes weaker with increase in distance from the melt region and finally nearly disappears at the chamber walls that are cooled by external coolant convection. We can thus assume that the core region

of a CZ growth furnace is characterized by three-dimensionality, and that the regions away from the core region are predominantly two-dimensional. In this study, the 3D domain, as shadowed in Fig. 1, includes the crystal, melt, crucible and heater, while the other regions in the furnace are included in the 2D domain. As a result, a local view of the computation grid system is as shown in Fig. 2.

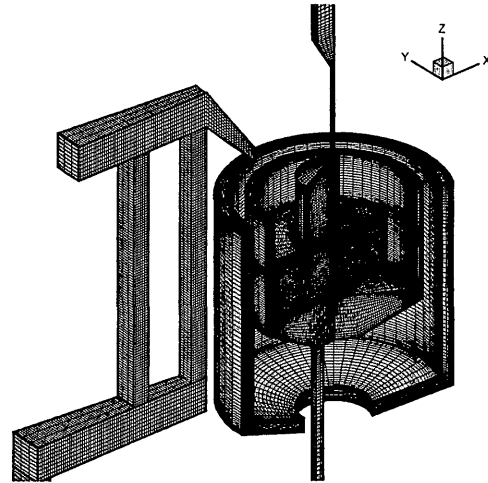


Fig. 2 A local view of the computation grid system

By doing so, the computation time and the memory requirement for 3D global modeling decrease dramatically, enabling 3D global modeling with moderate requirement of computer resources and permissible computation time. Furthermore, in order to improve the preciseness of computation, the grids are refined with special attention to places close to interfaces or boundaries, to places with abrupt changes in physical properties or geometry.

2.2 Governing equations of the thermal system

The global modeling of heat transfer in the furnace involves the convective heat transfer of melt in the crucible, the conductive heat transfer in all solid components and the radiative heat transfer in all enclosures of the furnace, while the effect of gas flow in the furnace is neglected in the model. The growth system is assumed to be quasi-steady. The melt flow is assumed to be incompressible and laminar.

With these assumptions, the mass conservation, momentum and energy equations for the thermal flow of melt in a crucible under the influence of a magnetic field can be generally written as follows:

$$\nabla \cdot \vec{V} = 0, \quad (1)$$

$$\rho \vec{V} \cdot \nabla \vec{V} = -\nabla p + \nabla \cdot \left[\frac{1}{2} \mu (\nabla \vec{V} + \nabla \vec{V}^T) \right] - \rho \bar{g} \beta_T (T - T_m) + \vec{J} \times \vec{B}, \quad (2)$$

$$\rho c \vec{V} \cdot \nabla T = \nabla \cdot (k \nabla T), \quad (3)$$

where β_T is the thermal expansion coefficient of molten silicon, T_m is the freezing temperature of molten silicon, \vec{B} is the magnetic flux density applied and \vec{J} is the electrical current density that the magnetic field induced. The last two terms in equation (2) are the thermal buoyancy force and the Lorentz force.

In order to determine the Lorentz force exerted on the molten silicon, we need to solve the electrical field induced by the imposed magnetic field, which is governed by

$$\nabla \cdot \vec{J} = 0, \quad (4)$$

$$\vec{J} = \sigma_m (\vec{E} + \vec{U}_M \times \vec{B}) \quad \text{in the melt}, \quad (5.1)$$

$$\vec{J} = \sigma_s (\vec{E} + \vec{U}_M \times \vec{B}) \quad \text{in the crystal}, \quad (5.2)$$

$$\vec{E} = -\nabla \Phi, \quad (6)$$

where \vec{E} is the electric field, Φ is the electrical potential, U_M is the relative velocity of melt or crystal to the magnetic field, σ_m and σ_s are the electrical conductivities of molten silicon and crystal, respectively. The effect of the induced magnetic field on the applied field is neglected. The crucible, pulling rod and ambient gas are electrically insulated, while the silicon crystal is an electrical conductor. Therefore, the calculation of electromagnetic field is limited to the melt-crystal domain.

The heat is transported by the mode of conduction in solid components in the furnace. The heat transfer in the heater is governed by

$$\nabla \cdot (k_h \nabla T) + S_Q = 0, \quad (7)$$

where S_Q is the heat source per unit volume in the heater. The governing equations for the thermal fields in other solid components are in the form

$$\rho_i c_i \vec{V}_i \cdot \nabla T = \nabla \cdot (k_i \nabla T), \quad (8)$$

where the subscript i represents respective components and \vec{V}_i is the advection velocity. These solid components include the crystal, crucible, pulling rod, pedestal and heat insulators.

Finite volume calculations were carried out for the melt flow in the crucible and thermal fields in all solid components with a discretization on nonorthogonal grids.

Radiative heat exchange plays a major role in heat transport within a CZ-Si growth furnace. Modeling of radiative heat transfer in radiation enclosures of a CZ furnace is an important part of global simulation. In our model, the radiative heat exchange in radiative enclosures is modeled on the basis of an assumption of diffuse-gray surface radiation. Let ∂V stand for a radiative enclosure. The surface temperature $T(\vec{x})$ and the net heat flux $q(\vec{x})$ on the enclosure surfaces are related by the following integral relationship:

$$\frac{q(\vec{x})}{\varepsilon(\vec{x})} - \int_{\vec{x}^* \in \partial V} K(\vec{x}, \vec{x}^*) \frac{1 - \varepsilon(\vec{x}^*)}{\varepsilon(\vec{x}^*)} q(\vec{x}^*) dS^* = \sigma T^4(\vec{x}) - \int_{\vec{x}^* \in \partial V} K(\vec{x}, \vec{x}^*) \sigma T^4(\vec{x}^*) dS^*, \quad (9)$$

where ε is the radiative emissivity of the enclosure surfaces, σ is the Stefan-Boltzmann constant, \vec{x} and \vec{x}^* are infinitesimal radiative surface elements on the enclosure ∂V , and dS^* is the area of the infinitesimal surface element \vec{x}^* . $K(\vec{x}, \vec{x}^*)$ is the surface view factor between \vec{x} and \vec{x}^* . Whenever \vec{x} and \vec{x}^* face each other, it is given by the following formula:

$$K(\vec{x}, \vec{x}^*) = - \frac{[(\vec{x} - \vec{x}^*) \cdot \vec{n}][(\vec{x} - \vec{x}^*) \cdot \vec{n}^*]}{\pi [(\vec{x} - \vec{x}^*) \cdot (\vec{x} - \vec{x}^*)]^2}, \quad (10)$$

where \vec{n} and \vec{n}^* are unit vectors normal to the infinitesimal areas dS and dS^* at \vec{x} and \vec{x}^* , respectively. Otherwise, when \vec{x} and \vec{x}^* do not face each other, it equals zero.

For any finite radiative surface element $\vec{X} \in \partial V$, which is consistent with the surface grid of a component on which the radiative surface belongs to, equation (9) can be rewritten in a compact form as follows, after many trivial manipulations by considering the assumptions applied and the discrete grid system designed in the model⁷⁾:

$$\frac{q(X)}{\varepsilon(X)} - \sigma T^4(X) = \sum_{i=1}^{NT} \frac{1 - \varepsilon(X_i)}{\varepsilon(X_i)} q(X_i) K_e(X, X_i) r_{ic} \Delta s_i - \sum_{i=1}^{NT} \sigma T^4(X_i) K_e(X, X_i) r_{ic} \Delta s_i, \quad (11)$$

where NT is the total number of radiative surface element of an enclosure, r_{ic} and Δs_i are the radius and the length of the circumferential projection of the surface element X_i , respectively. The view factor $K_e(X, X_i)$ between two finite radiative surface elements is calculated as follows:

when $X_i \in \partial V^2$,

$$K_e(X, X_i) = K_C(\bar{x}_c', \bar{x}_{ic}'), \quad (12.1)$$

when $X_i \in \partial V^3$ and $\bar{X} \in \partial V^2$,

$$K_e(X, X_i) = \frac{(\theta_{i2} - \theta_{i1})}{2\pi} K_C(\bar{x}_c', \bar{x}_{ic}'), \quad (12.2)$$

when $X_i \in \partial V^3$ and $\bar{X} \in \partial V^3$,

$$K_e(X, X_i) = \int_{\theta_{i1}}^{\theta_{i2}} K(\bar{x}_c', \bar{x}_i^*) d\theta^*, \quad (12.3)$$

where \bar{x}_c' and \bar{x}_{ic}' are the respective circumferential projections in a meridional plane of the geometrical centers or the representative points $\bar{x}_c \in X$ and $\bar{x}_{ic} \in X_i$. $(\theta_{i1}, \theta_{i2})$ is the angular width of the radiative surface element $X_i \in \partial V^3$ and $\bar{x}_i^* = (r_{ic}' \cos \theta^*, r_{ic}' \sin \theta^*, z_{ic}')$. $K_C(\bar{x}_c', \bar{x}_{ic}')$ is an axisymmetric view factor defined by the integral

$$K_C(\bar{x}_c', \bar{x}_{ic}') = \int_0^{2\pi} K(\bar{x}_c', \bar{x}_i^*) d\theta^*. \quad (13)$$

2.3 Implementation of the global modeling

The global model consists of a set of local iterations for each of these block regions and a global conjugated iteration amongst them. The global iteration is conducted through iteratively updating the thermal fields on the interfaces between every two adjacent regions and all radiative surfaces on the basis of the conditions of temperature continuity and heat balance across all these interfaces and radiative surfaces. The code requires only a set of input parameters to perform a global simulation by using this model. These input parameters are the furnace geometry, material properties of each component, coolant temperature, melt volume, crystal radius and crystal growth rate. The heater input power and the melt-crystal interface shape are unknowns. They are solved iteratively in the global solution. The heater input power is determined in such a way that it is modified iteratively in the global iteration until the mean temperature over the tri-junction edge approaches the

freezing point of molten silicon. The melt-crystal interface shape is determined in such a way that it is updated iteratively in the global iteration until the temperature on the interface consistently approaches the freezing point of molten silicon. That is, we track the melt-crystal interface with identification to an isothermal face of the freezing point of molten silicon.

In order to speed up the iteration convergence, a 2D global simulation in the absence of a magnetic field, which is feasible and can be completed in a short computation time, is carried out for obtaining the initial fields in the furnace and the initial value of heater input power. This technique results in dramatic decrease in computation time of 3D global iteration.

The iteration procedure of the global solution is outlined as follows.

1) Carry out a 2D global simulation in the absence of a magnetic field. The solution of the 2D global simulation is taken as the initial fields, the initial melt-crystal interface position and the initial value of the heater input power for the following 3D global iteration.

2) Solve the melt flow, thermal field and electromagnetic field in the melt-crystal domain with a fixed melt-crystal interface shape.

3) Solve the thermal fields in all of the other solid conductive block regions.

4) Renew the thermal fields on the interfaces between every two adjacent block regions and all radiative surfaces.

5) Calculate the radiative heat transfer in all radiative enclosures of the furnace.

6) Renew the thermal field on all radiative surfaces.

7) Check the convergence of the global iteration. If it has not converged, return to step 2) and continue to the next global iteration. If it has converged, proceed to step 8).

8) Check the convergence of the heater input power. If it has not converged, renew it and then return to step 2) and continue to the next cycle of computation. If it has converged, proceed to step 9).

9) Check the convergence of the melt-crystal interface location. If it has not converged, modify it. Adjust the computation grids in the melt-crystal domain to fit the new interface shape. Interpolate the present solutions on the new grids as the initial field for the next iteration. Then return to step 2) and continue to the next cycle of computation. If the melt-crystal interface location has converged, terminate the computation and output the converged results.

3. Results and discussion

Simulations were carried out for a small silicon CZ growth furnace, as illustrated in Fig. 1, for cases in which the crystal and crucible are not rotating or rotate at high speeds, respectively. The magnetic field is homogeneous with intensity of 0.1 T oriented in the X-direction. The crystal diameter is 32 mm. The diameter of the crucible inside wall is 64 mm. The depth of the melt is 28 mm. A typical crystal growth rate of 0.3 mm/min is applied. The material properties of the constituents of the furnace are listed in Table 1. The 3D domain includes the crystal, melt, crucible and heater. The discrete system is constituted by about 370,000 control volumes and 24,000 radiative surface elements. A computation run takes about ten days on a HP ITANIUM 2 workstation with memory capacity of 2.6 gigabytes.

Table 1 Material property parameters of the constituents of the furnace

Density

$$\begin{aligned} \rho &= 2520 \text{ kg/m}^3 \text{ (melt),} \\ \rho &= 2305 \text{ kg/m}^3 \text{ (crystal),} \\ \rho &= 2190 \text{ kg/m}^3 \text{ (quartz crucible),} \\ \rho &= 2262 \text{ kg/m}^3 \text{ (heater, pedestal, seed/puller, heat} \\ &\quad \text{insulators)} \end{aligned}$$

Thermal conductivity

$$\begin{aligned} k &= 54 \text{ W/m}\cdot\text{K} \text{ (melt),} \\ k &= 25.7 \text{ W/m}\cdot\text{K} \text{ (crystal),} \\ k &= 5.0 \text{ W/m}\cdot\text{K} \text{ (quartz crucible),} \\ k &= 42 \text{ W/m}\cdot\text{K} \text{ (heater, pedestal, seed/puller, heat} \\ &\quad \text{insulators)} \end{aligned}$$

Heat capacity

$$\begin{aligned} c &= 1000 \text{ J/kg}\cdot\text{K} \text{ (melt),} \\ c &= 946 \text{ J/kg}\cdot\text{K} \text{ (crystal),} \\ c &= 1525 \text{ J/kg}\cdot\text{K} \text{ (quartz crucible),} \\ c &= 2050 \text{ J/kg}\cdot\text{K} \text{ (heater, pedestal, seed/puller,} \\ &\quad \text{heat insulators)} \end{aligned}$$

Emissivity factor

$$\begin{aligned} \varepsilon &= 0.30 \text{ (melt), } \varepsilon = 0.58 \text{ (crystal),} \\ \varepsilon &= 0.35 \text{ (chamber walls),} \\ \varepsilon &= 0.50 \text{ (quartz crucible),} \\ \varepsilon &= 0.80 \text{ (heater, pedestal, seed/puller, heat} \\ &\quad \text{insulators)} \end{aligned}$$

Electrical conductivity

$$\begin{aligned} \sigma_m &= 1.29 \times 10^6 \text{ S/m} \text{ (melt),} \\ \sigma_s &= 1.20 \times 10^5 \text{ S/m} \text{ (crystal)} \end{aligned}$$

Freezing temperature of molten silicon

$$T_m = 1685 \text{ K}$$

Thermal expansion coefficient of melt

$$\beta_T = 1.4 \times 10^{-4} \text{ K}^{-1}$$

Latent heat of solidification

$$\Delta H = 1411 \times 10^3 \text{ J/kg}$$

Dynamic viscosity of melt

$$\mu = 7.0 \times 10^{-4} \text{ kg/m}\cdot\text{s}$$

Coolant temperature $T_w = 350 \text{ K}$

Stefan-Boltzmann constant

$$\sigma = 5.6696 \times 10^{-8} \text{ W}\cdot\text{m}^{-2}\cdot\text{K}^{-4}$$

3.1 Analysis of a TMCZ growth process with non-rotating crystal and crucible

Fig. 3 through Fig. 6 show some results obtained by 3D global modeling for a silicon TMCZ process with non-rotating crystal and crucible. The converged heater power is 16.0 kW in this test case. The local temperature distribution in the core regions of the furnace is shown in Fig. 3. The thermal field is symmetric about both plane $x=0$ and plane $y=0$. However, it is apparent that the thermal field in the core regions is characterized by three-dimensionality, especially in the melt. Even the inhomogeneity of temperature distribution in the azimuthal direction on the outside wall of crucible is noticeable. Fig. 4 shows the convective flow patterns of melt and temperature distributions in three representative planes that are respectively located at 5%, 50% and 95% depth of melt in the crucible. Under the combined influence of the thermal buoyancy and the transverse magnetic field, the

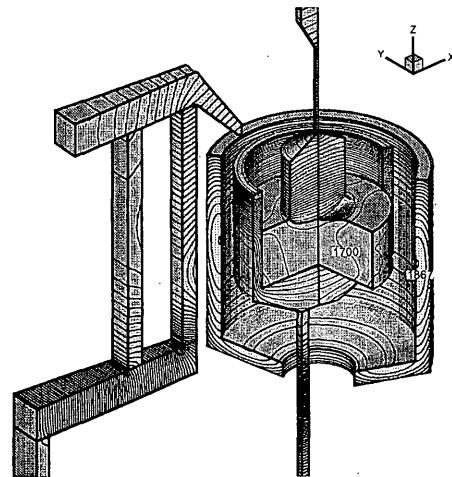


Fig. 3 Local temperature distribution in the core regions of a furnace. Isotherms are plotted every 11 K.

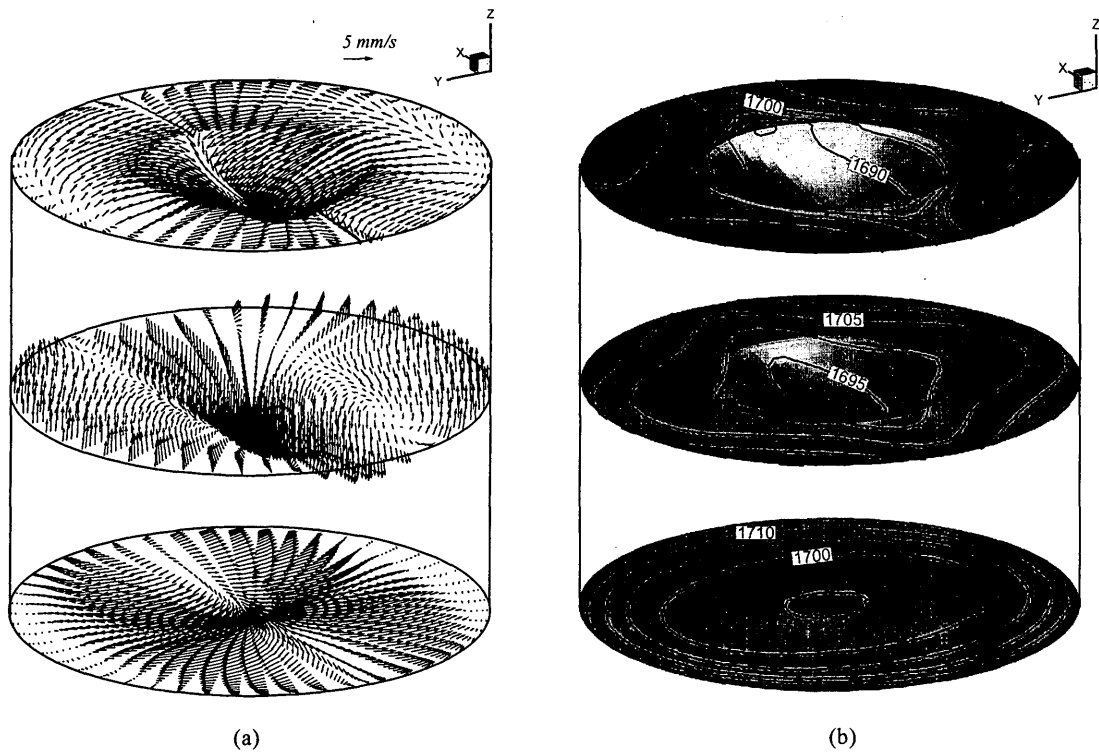


Fig. 4 Convective flow patterns and temperature distributions in three planes at 5%, 50% and 95% depth of melt (from top to bottom). (a) Convective melt flow. (b) Temperature distribution. Isotherms are plotted every 5 K.

melt flows upward along the crucible sidewall in regions that are away from the symmetric plane $y = 0$, then flows toward it at the melt surface, and finally sinks down to the crucible bottom in this symmetric plane. A pair of strong convective vortices is thus generated in the symmetric plane $x = 0$ and the melt almost flows downward in the plane $y = 0$. Corresponding to the three-dimensional convective flow pattern of melt, the temperature distributions in the half-planes $x = 0$ and $y = 0$, as shown in Fig. 3, and the temperature distributions in the three horizontal planes at different depths in the melt, as shown in Fig. 4 (b), are distinctly different.

Fig. 5 shows a 3D view of the melt-crystal interface and the temperature distribution on the melt top surface as well as on the interface. As a result of the three-dimensional feature of the convective flow and thermal field in the melt, the melt-crystal interface is also characterized by distinct three-dimensionality. An elliptic region of low temperature is generated on the melt surface in the magnetic field direction, resulting in the ridge of the interface in the X-direction.

In order to examine the non-uniformity of the thermal field in the azimuthal direction, a few typical

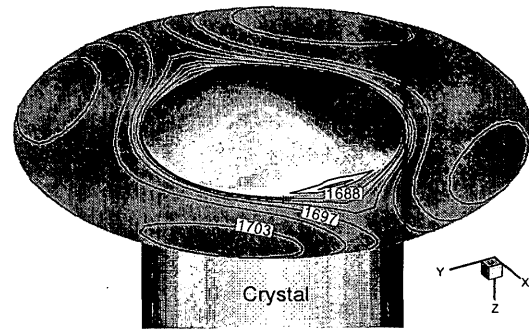


Fig. 5 A 3D view of the melt-crystal interface and the temperature distribution on the melt top surface as well as on the interface. Isotherms are plotted every 3 K.

monitoring locations were selected for study. These monitoring locations are on the crystal sidewall, the melt surface, the melt bottom, the melt sidewall, and the crucible outside wall, as illustrated in Fig. 6 (a). The temperature distributions in the azimuthal direction at these locations are shown in Fig. 6 (b). Distinct non-uniformity of the temperature distribution can be

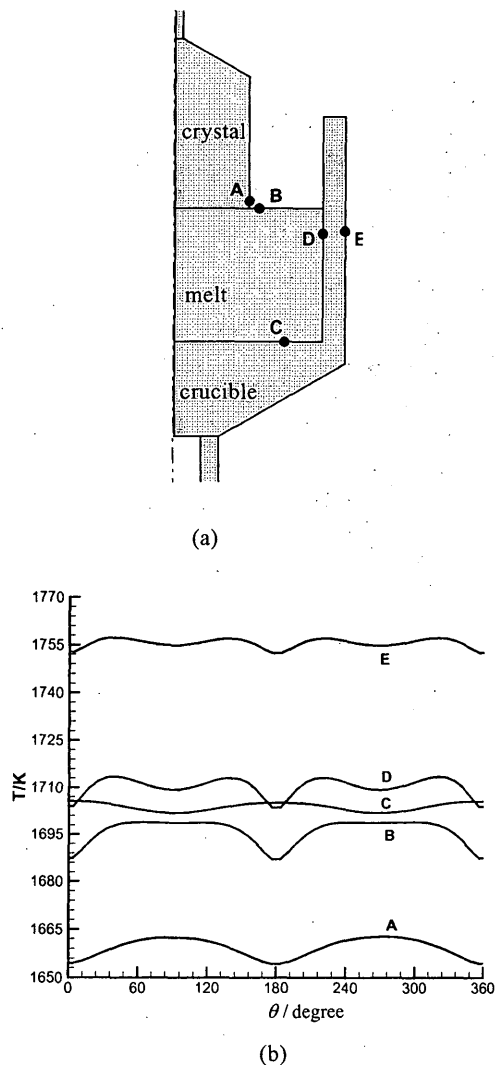


Fig. 6 Non-uniform temperature distributions in the azimuthal direction. (a) Locations under consideration. (b) A, the crystal sidewall; B, the melt top surface; C, the melt bottom; D, the melt sidewall; E, the crucible outside wall.

observed in the azimuthal direction. The maximal difference in temperature over the circumference occurs on the melt surface with a value as high as 13.2 K. Meanwhile, the non-uniformity is small at the melt bottom (curve C) compared to that at the melt surface (curve B) and that at the melt sidewall (curve D), and this non-uniformity decreases further with increase in distance from the melt domain. This can be confirmed from Fig. 6 (b), in which it can be seen that the non-uniformity of 10.0 K at the melt sidewall (location D) decreases to 4.9 K at the outside wall of the crucible (location E).

3.2 Analysis of a TMCZ growth process with rotating crystal and crucible

Fig. 7 through Fig. 9 show the results obtained by 3D global modeling for a silicon TMCZ process in which the crystal rotates at 30 rpm and the crucible rotates at -5 rpm. Fig. 7 shows the convective flow patterns and temperature distributions of melt in three horizontal planes. Compared with the corresponding results obtained for the case in which the crystal and crucible are not rotating, as shown in Fig. 4, the melt flow pattern under the melt top surface and the melt-crystal interface are more complex due to the combined influence of the transverse magnetic field and the crystal and crucible rotations. A pair of vortices is generated under the melt-crystal interface in the horizontal direction, as can be seen in Fig. 7 (a). Accordingly, the temperature distribution patterns in these planes are different from those shown in Fig. 4 (b) for the case with non-rotating crystal and crucible, and the maximal temperature difference in the melt is larger. The deformedly elliptic region of low temperature is oriented in the direction of the magnetic field under the melt surface, but in the perpendicular direction at the bottom. Both the velocity and temperature fields are no longer symmetric to the symmetric planes $x=0$ and $y=0$. However, they are symmetric to the axis of crucible.

Fig. 8 is a 3D view of the melt-crystal interface shape and the temperature distribution on the melt top surface as well as on the melt-crystal interface. Differing from the three-dimensional interface shape shown in Fig. 5 for the case in which the crystal and crucible are not rotating, the deflection of melt-crystal interface shape is almost uniform over circumference in this case, as can be observed in Fig. 8, though the melt flow and thermal field are three-dimensional. This indicates that the crystal and crucible rotations homogenize the melt-crystal interface deflection over circumference.

The non-uniformity of temperature distribution in the azimuthal direction under this condition is examined in Fig. 9. Comparing to the case in which the crystal and crucible are not rotating, as shown in Fig. 6 (b), distinct non-uniformity of the azimuthal temperature distribution can also be seen in the melt. However, the non-uniformities of azimuthal temperature distribution on the crystal and crucible outside walls become much weaker due to the crystal and crucible rotations. The temperatures on the inside and bottom walls of crucible are slightly higher. Meanwhile, the overheating of the

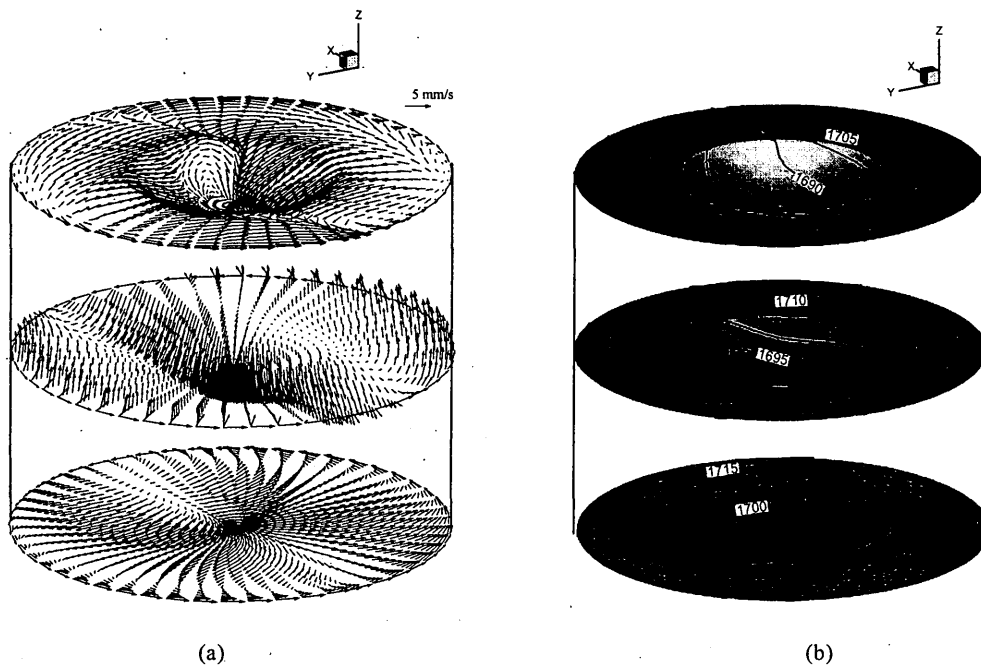


Fig. 7 Convective flow patterns and temperature distributions in three planes at 5%, 50% and 95% depth of melt (from top to bottom) for the case in which the crystal and crucible rotate. (a) Convective melt flow. (b) Temperature distribution. Isotherms are plotted every 5 K.

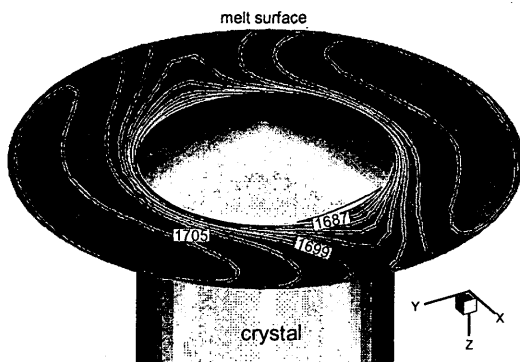


Fig. 8 A 3D view of the melt-crystal interface and the temperature distribution on the melt top surface as well as on the interface for the case in which the crystal and crucible rotate. Isotherms are plotted every 3 K.

crucible outside wall is about 4 K lower. The converged heater power under this condition is 15.9 kW, slightly lower than that of the former case with non-rotating crystal and crucible.

4. Conclusions

3D global analyses were conducted using a developed model for a silicon TMCZ growth furnace for

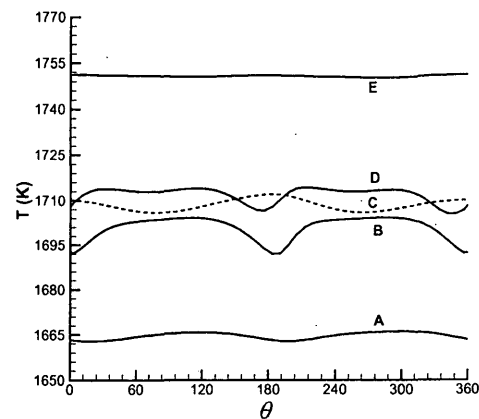


Fig. 9 Non-uniform temperature distributions in the azimuthal direction for the case in which the crystal and crucible rotate. A, the crystal sidewall; B, the melt top surface; C, the melt bottom; D, the melt sidewall; E, the crucible outside wall.

the cases in which the crystal and crucible are not rotating or rotate at high speeds, respectively. The numerical simulations were conducted with moderate requirements of computer resources and computation time. Three-dimensional features of the melt flow in the crucible and the thermal field in the furnace, along

with the melt-crystal interface shape, were reasonably reproduced in the simulations.

The melt flow pattern and thermal field are more complex under the combined influence of a transverse magnetic field and the crystal and crucible rotations. Comparing to the case in which the crucible and crystal are not rotating, it was found that the melt-crystal interface deflection is almost homogenized over circumference and the azimuthal temperature non-uniformity is much weaker on the crystal and crucible outside walls at high rotation rates of crucible and crystal.

Acknowledgements

This work was supported by a Grant-in Aid for Scientific Research (B) 14350010 from the Japanese Ministry of Education, Science, Sports and Culture.

References

- 1) K. Kakimoto, Oxygen distribution in silicon melt under inhomogeneous transverse magnetic fields, *J. Crystal Growth* 230 (2001) 100-107
- 2) K. Kakimoto, A. Tashiro, T. Shinozaki, H. Ishii, Y. Hashimoto, Mechanisms of heat and oxygen transfer in silicon melt in an electromagnetic Czochralski system, *J. Crystal Growth* 243 (2002) 55-65.
- 3) K. Kakimoto, Effects of rotating magnetic fields on temperature and oxygen distributions in silicon melt, *J. Crystal Growth* 237-239 (2002) 1785-1790.
- 4) H. Ozoe, M. Iwamoto, Combined effects of crucible rotation and horizontal magnetic field on dopant concentration in a Czochralski melt, *J. Crystal Growth* 142 (1994) 236-244.
- 5) A. Krauze, A. Muiznieks, A. Muhlbauer, Th. Wetzel, W.v. Ammon, Numerical 3D modeling of turbulent melt flow in a large CZ system with horizontal DC magnetic field, I: flow structure analysis, *J. Crystal Growth* 262 (2004) 157-167.
- 6) A. Krauze, A. Muiznieks, A. Muhlbauer, Th. Wetzel, E. Tomzig, L. Gorbunov, A. Pedchenko, J. Virbulis, Numerical 3D modeling of turbulent melt flow in a large CZ system with horizontal DC magnetic field, II: comparison with measurements, *J. Crystal Growth* 265 (2004) 14-27.
- 7) L.J. Liu, K. Kakimoto, Three-dimensional global modeling of a silicon Czochralski furnace I. Principles, Formulation and Implementation of the Model, *Int. J. Heat Mass Transfer*, submitted for publication, 2004